SIS SHARDS

ACE Memo ID: 1997.02.01.BLD.a (JPL/SIS/detector thickness calibrations)

From: Brian L. Dougherty (bld@heag1.jpl.nasa.gov)

To: CRIS/SIS Data Analysis Teams

Date: 1 Feb. 1997

inre: Mechanical measurements of the absolute thickness of silicon offcuts were made to compare with earlier measurements of residual energies of a penetrating ^{36}Ar beam, and so calibrate the thickness of our SIS detectors.

In SIS we derive incoming particle masses from measurements of energy deposited in the stack detectors. The mass resolution depends on a precise knowledge of a number of different physical variables, but of particular concern in this memo is our need for maps of the stack-detector thicknesses that are accurate to within 0.3%.

Relative-thickness maps were made at JPL using a two-arm laser interferometer. These are the subject of a separate report by Mark Wiedenbeck.

Measurements of residual energy through selected spots on each detector were made using an ^{36}Ar beam at the MSU NSCL. Bruce Sears did the analysis.

This memo supplies the residual energy -to- absolute thickness calibration needed to relate the above two data sets. We cannot use standard range-energy tabulations since our experimental uncertainties and systematics (e.g. total incident beam energy, electronics gain, etc.) were not known well enough. Instead, we compare the empirically determined residual energy and absolute thickness for a number of auxiliary silicon samples which are of similar thickness as the detectors. We used the offcuts (or "shards") that Micron Semiconductor took from the edges of processed detectors (see Figure 1). These were exposed to the same ^{36}Ar beam, and Bruce has provided the residual energy measurements that will be employed later. The last remaining need, and the subject of the bulk of this rather lengthy report, is for determinations of the absolute thicknesses of these shards. An accuracy of around 0.1 μm is desired, which is roughly ten times better then the precision of a typical micrometer.

My motive for writing a longer, detailed memo is that it prooved difficult to find a way to make such measurements. Many electro-mechanical and optical means were explored, but none were as accurate, practicable, or simple as the "off the shelf" mechanical method described here. (Final results may be found on page 18.)

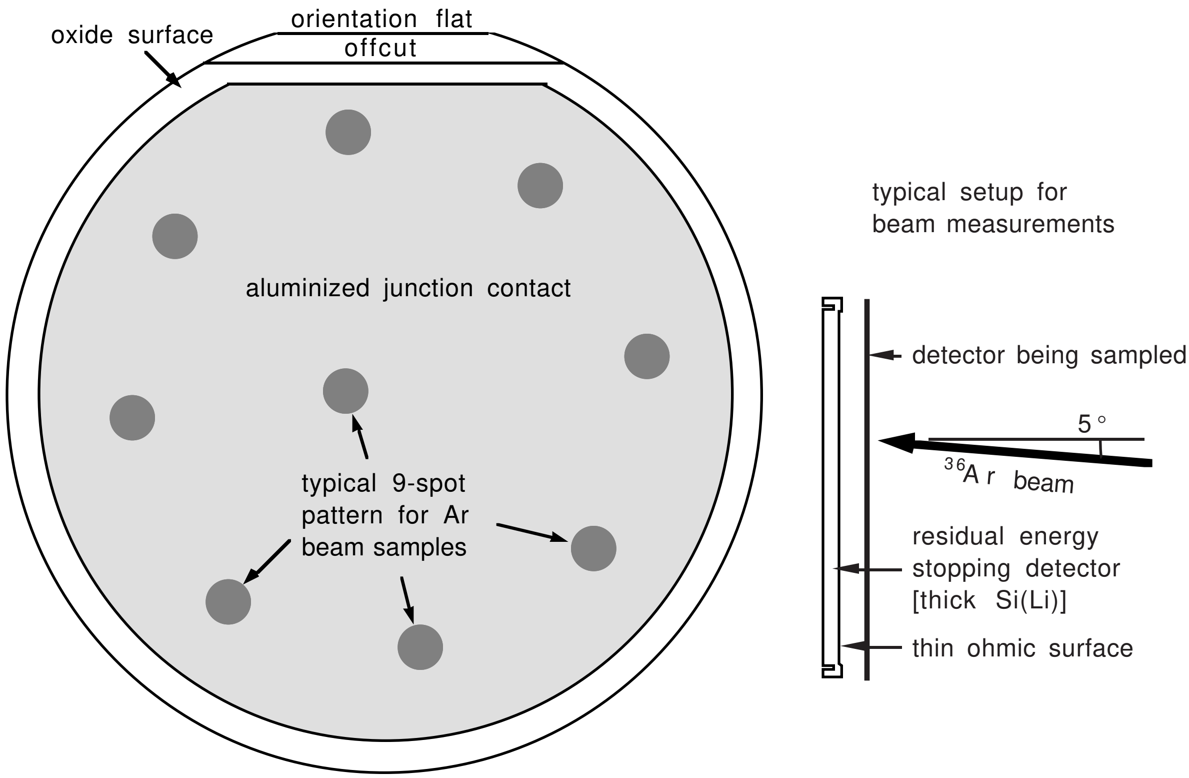

Figure 1. Scale view of a SIS detector, with location of offcut shown, and typical positions of 9 sampling spots for measurements of residual beam energy. The spot spacing was held constant, while the asymuthal orientation was randomized.

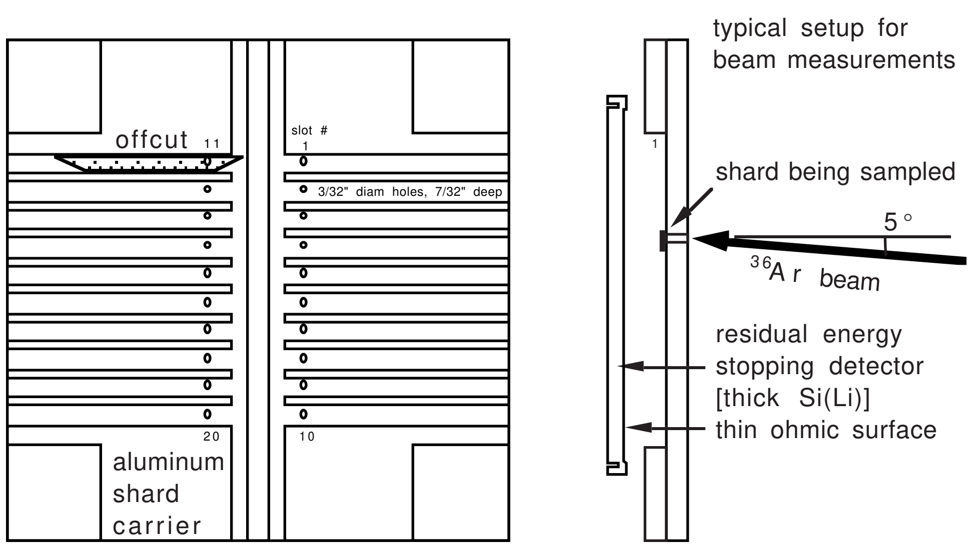

Figure 2. Half-scale view of the carrier used to make residual-energy measurements of the ^{36}Ar beam that passed through the shards, which were tacked in place with silicone over 3/32" diameter hole collimators.

The offcuts/shards generally have oxide layers on one side, and vacuum-deposited aluminum on the other. Both surfaces are specular. As shown in Figure 2, shards were attached to carriers which have holes used to collimate the ^{36}Ar beam. To avoid channelling effects, detectors and carriers were tilted 5° (nominally) with respect to the beam. Detector thicknesses were sampled at 9 spots. The same beam and stopping detectors were used throughout to measure residual energies. The same air gap (silicon specimen -to- stopping detector distance) was maintained. The beam was not collimated, however, when we sampled the detectors. Also, the shards were not guarranteed to lie flat against the bottom of their carrier slots. A tilt slightly different than 5° may have resulted. If such θ's were random in size as well as sign (either adding or subtracting from 5° for different shards) then the random secθ errors would effect our thickness uncertainties, without compromising the average trends. Systematic deviations could not be ruled out, however, so it became important to measure shard thicknesses in-situ, with tilts preserved.

A Heidenhain CERTO CT60M gauge was found and made available at Barry Controls Aerospace in Burbank. Preliminary tests with a series of gauge blocks indicated that its advertised accuracy of ± 0.1 μm was indeed attainable. Probe movements of 2 inches could be made with very good repeatability. There were no warm-up drifts.

Figure 3 shows the setup used to measure shards. The gauge and stand were already at Barry Controls. We augmented these with a thick steel fixture. The heft of this fixture was needed to minimize any errors due to flexing. A steel pin of 2 mm diameter, made from a stainless screw, stuck up through the surface of this fixture. Its height was adjusted to rise above the slot surface of a shard carrier by ≈ 0.5 mm when penetrating any one of the collimator holes. It was locked in place with a nut under the fixture. Its tip had been coaxially rounded on a lathe, and hand polished to a mirror surface with a radius of about 1.7 mm (± 10 %).

All metal surfaces were first cleaned with alcohol, and the steel fixture was "wrung" down on the granite base. The pin was then carefully aligned with the probe shaft, itself tipped with a 3 mm diameter steel ball. This was done by letting the probe tip rest on the pin, and watching the continuously metered gauge height change while tapping the fixture from side to side. With alternating front-back and left-right taps, the highest point on the pin was found to well within the finest readout scale on the meter (0.05 μm). This is equivalent to locating the crown laterally to within 18 μm (see Figure 5). A vacuum was then applied to a groove at the bottom of the steel fixture. The readout did not change; i.e. the wring had been successful. Thereafter, no change in readout could be induced by pushing on the pin itself, or by rapping and shoving on the fixture. The meter was then zeroed, and never again reset. Regular checking allowed any drifts to be followed.

Figure 3. Setup for use of the Heidenhain gauge.

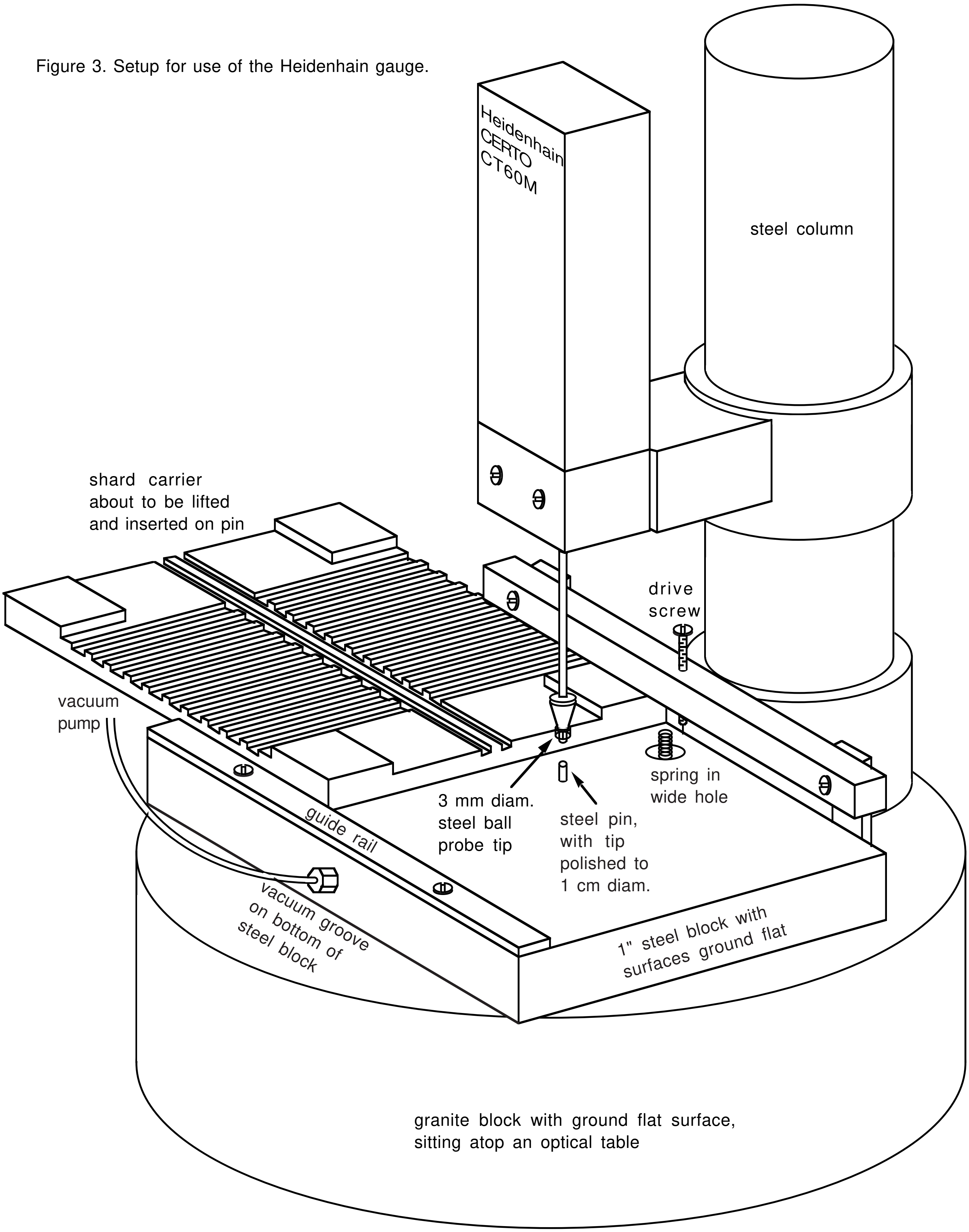

A measurement was set up by butting a carrier against the guide rail and supporting one edge off the fixture surface by resting it on the spring, all the while aligning so that the pin slipped loosely through a collimator hole. The tilted carrier was then driven slowly down with a hand-turned screw until a pin "touch" could be confirmed with the bottom of the shard. This was done by watching reflections in the shard surface, from a distance of roughly 8 inches overhead, and noting when images started to move. Shard distortions and extra tilts were kept below any range of concern by delimiting reflection movements to less than 1 mm. Design details can be seen in Figure 4. Figure 5 clarifies error sources.

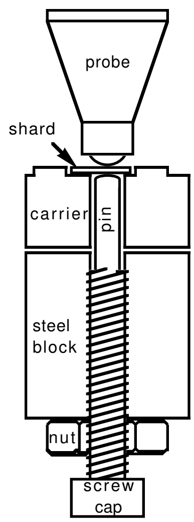

Figure 4. Details of the thickness measurment. The pin is adjusted in height and locked in place by tightening the nut. The carrier is slowly lowered, with the pin through a hole, until a "touch" is seen in the movement of reflections off the shard. When the probe is dropped, a distinct click can be heard if good contact is made to both sides of the shard.

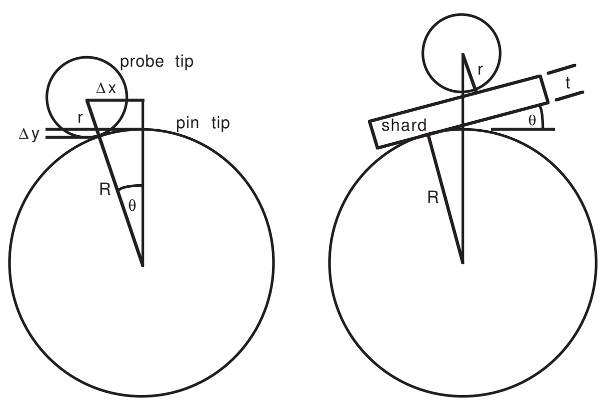

Figure 5. Dominant sources of error. The probe and pin tips are represented as circles of very different radii. To the left is a transverse displacement of tips by Δx, leading to a "zero" thickness calibration that is too low by $\Delta y = (1 - \cos\theta)(r + R)$. For small θ this aproximates $\Delta y \approx (\Delta x)^2/2(r + R)$. To the right is a tilted shard, leading to an over-measurement by $\Delta y = (\sec\theta - 1)(r + R + t) \approx \theta^2(r + R + t)/2$.

The probe was then brought down with a switch-settable force of 1.75 N. A distinct, high-pitched click could be heard when good contact was made to both sides of a shard. Probe motion was controlled by a toggle, and it prooved important to release this switch just as contact was made, to let the probe automatically reach its measuring force. Shard reflections did not move when a "touch" was accomplished correctly. Toggling the probe up and down confirmed a viable setup. Four measurements where then taken, one right after another. Repeatability was good, typically within 0.1 μm.

The entire set of raw measurements can be perused in Table 1, listed in the order in which they were taken. (We show all the data to display its consistency, and thus how finely cuts can be made.) There were five carriers with twenty shards apiece. A sixth carrier was loaded with four steel gauge blocks and one other silicon shard. This carrier was used repeatedly to check for linearity and stability. The nominal thicknesses of the gauge blocks were 100, 250, 500, and 1000 μm. "Zero" was re-checked after every tenth shard by dropping the probe onto an empty pin.

It took three hours to measure all the shards once. Several samples were then remeasured to assess repeatability: second averages tended to differ by less than 0.15 μm from the first. Problems met along the way are noted in the "comment" column of the table, along with remarks in parentheses that indicate data that did not pass cuts applied later. The comment "rep" is used to flag shards with bad repeatability. Data with rms deviations of more than 0.05 μm are flagged by "sig". Successive measurements which changed too rapidly are flagged by "slp": only average slopes between –0.02 and 0.04 μm per probe hit were accepted. The mean rate of change for all shards was 0.007 ± 0.024 μm per hit: i.e. they tended to appear slightly thicker as the 4 measurements progressed (see Figure 6). Since these changes are so small, this is not a concern, but such slopes do indicate that the shards may have been tilting in their mounts as the probe jostled them. In all, 18 out of 176 sets of 4 measurements were eliminated with these cuts, including some calibrations.

A seen in Figure 7a, the "zero" calibrations moved about very little, typically by less than ~ 0.05 μm, or the finest division available in readout. They did, however, appear to shift downward by ≈ 0.075 μm after the fourth check. Figure 7b shows that the gauge blocks tended to follow these "zero" shifts, as well as one another's thickness-changing trends. These effects could have been due to a metering drift or an abrasion of the steel pin. (A lateral movement of the pin would not result in a common trend.) In any case, we compensate for these slight shifts by subtracting from any measurement the zero calibration taken just previously to it.

Table 1. Raw Data

carrier	slot	shard ID	meas #1	meas #2	meas #3	meas #4	comment
calib.	1	1000 µm	1000.25	1000.25	1000.25	1000.30	9:15
calib.	3	500 µm	499.95	500.00	500.00	500.05	
calib.	5	250 µm	249.90	250.00	250.05	250.00	(sig)
calib.	7	100 µm	100.20	100.15	100.20	100.20	
calib.	9	0 µm	0.00	0.00	0.05	0.05	
calib.	10	1375-19	748.15	748.30	748.30	748.25	(sig)
1	1	1280-21	964.65	964.60	964.70	965.15	(rep,sig,slp)
1	2	1021-10	984.10	984.15	984.20	984.20	
1	3	1280-3					out of mount
1	4	1280-15	969.25	969.30	969.30	969.25	
1	5	1141-1	979.50	979.65	979.65	979.60	(sig)
1	6	1021-14	971.85	971.90	971.90	971.90	
1	7	1020-10	975.45	975.50	975.55	975.50	
1	8	1141-2	975.35	975.35	975.35	975.40	
1	9	1280-9	973.70	973.75	973.85	973.80	(sig,slp)
1	10	1259-2	984.75	984.75	984.80	984.75	
—		0 µm	0.00	0.00	0.00		
1	11	1279-21	891.85	891.90	891.90	891.90	
1	12	1280-22	988.35	988.35	988.35	988.35	
1	13	1280-18	989.20	989.20	989.20	989.20	
1	14	1331-2	991.80	991.80	991.80	991.85	
1	15	1020-6	992.25	992.30	992.20	992.20	near crack (slp)
1	16	1225-6	991.75	991.80	991.80	991.80	
1	17	1331-11	968.45	968.50	968.50	968.45	
1	18	985-9	1005.10	1005.05	1005.10	1005.15	
1	19	1145-1	1006.75	1006.80	1006.75	1006.75	
1	20	1145-4	1010.95	1010.95	1010.95	1010.95	
calib.	1	1000 µm	1000.35	1000.35	1000.40	1000.35	9:55
calib.	3	500 µm	500.00	500.05	500.05	500.05	
calib.	5	250 µm	249.99	250.00	250.05	250.05	
calib.	7	100 µm	100.15	100.20	100.15	100.15	
calib.	9	0 µm	0.00	0.05	0.05	0.05	
calib.	10	1375-19	747.45	747.40	747.45	747.50	
2	1	1370-6	722.05	722.10	722.10	722.15	
2	2	1243-1	727.75	727.75	727.85	727.85	(sig,slp)
2	3	1317-18	729.35	729.35	729.40	729.40	
2	4	1370-41	731.10	731.15	731.15	731.10	
2	5	1242-4	738.05	738.15	738.05	738.10	
2	6	1317-6	745.70	745.70	745.70	745.75	
2	7	1242-3	760.60	760.55	760.60	760.60	
2	8	1243-3	754.60	754.65	754.65	754.60	
2	9	1317-9	759.20	759.25	759.25	759.25	
2	10	1342-20	796.25	796.30	796.25	796.25	
—		0 µm	0.00	0.05	0.05		
2	11	1279-10	886.15	886.20	886.20	886.20	
2	12	1281-4	883.15	883.20	883.25	883.25	
2	13	1279-22	894.15	894.15	894.15	894.10	
2	14	1281-1	894.05	894.05	894.10	894.05	
2	15	1279-4	892.35	892.40	892.45	892.40	
2	16	1279-23	894.60	894.55	894.65	894.60	
2	17	1279-6	903.75	903.80	903.75	903.80	
2	18	1279-14	901.25	901.30	901.25	901.25	
2	19	1279-18	897.05	897.10	897.10	897.10	
2	20	1279-8	915.30	915.25	915.25	915.20	(slp)
calib.	1	1000 µm	1000.25	1000.30	1000.25	1000.30	10:30
calib.	3	500 µm	499.90	499.95	499.95	499.90	
calib.	5	250 µm	249.95	249.95	249.95	250.00	
calib.	7	100 µm	100.10	100.15	100.10	100.10	
calib.	9	0 µm	-0.05	-0.05	-0.05	-0.05	
calib.	10	1375-19	747.90	747.90	747.95	747.85	
3	1	1276-16	501.00	501.05	501.00	501.00	
3	2	1110-21	472.65	472.65	472.75	472.70	
3	3	1098-5	476.70	476.75	476.70	476.75	
3	4	1098-7	477.05	477.10	477.10	477.15	
3	5	1111-17	487.65	487.70	487.65	487.70	
3	6	1110-20	483.00	483.05	482.95	483.05	
3	7	1276-19	489.45	489.55	489.50	489.50	
3	8	1276-14	481.85	481.95	481.95	481.90	
3	9	1276-20	484.70	484.75	484.75	484.80	
3	10	1111-21	481.95	481.95	482.00	482.00	
—		0 µm	-0.05	-0.05	-0.05		
3	11	1060-9	499.10	499.20	499.15	499.15	
3	12	1111-22	491.85	491.90	491.95	491.90	
3	13	1060-12	496.75	496.75	496.75	496.75	
3	14	1111-18	493.30	493.35	493.35	493.30	
3	15	1060-13	501.70	501.75	501.70	501.70	
3	16	1111-16	500.65	500.60	500.60	500.60	
3	17	1098-11	505.45	505.45	505.40	505.45	
3	18	1098-10	500.95	501.05	501.00	500.95	
3	19	1098-13	505.05	505.05	505.05	505.00	
3	20	1098-9	507.80	507.90	507.90	507.90	drags on pin
calib.	1	1000 µm	1000.25	1000.25	1000.30	1000.25	11:00
calib.	3	500 µm	499.95	499.95	499.95	499.95	
calib.	5	250 µm	249.95	249.95	249.95	249.95	
calib.	7	100 µm	100.05	100.05	100.00	100.05	
calib.	9	0 µm	-0.10	-0.05	-0.05	-0.05	
calib.	10	1375-19	746.50	746.55	746.50	746.50	

carrier	slot	shard ID	meas #1	meas #2	meas #3	meas #4	comment
4	1	1183-10	99.15	99.25	99.20	99.20	
4	2	1303-8	102.25	102.35	102.35	102.40	(sig,slp)
4	3	1183-3	94.70	94.70	94.70	94.70	
4	4	1083-9	100.65	100.65	100.65	100.65	
4	5	1083-7	101.20	101.25	101.25	101.25	
4	6	1183-7	99.60	99.60	99.60	99.65	
4	7	1303-20	100.25	100.30	100.25	100.25	(rep)
4	8	1303-2	99.35	99.35	99.40	99.45	
4	9	1083-8	99.85	99.95	99.95	99.95	
4	10	1183-2	99.25	99.25	99.25	99.25	
—		0 µm	-0.05	-0.05	-0.05		
4	11	1183-17	97.85	97.80	97.85	97.85	
4	12	1097-8	251.15	251.15	251.10	251.15	
4	13	1097-7	241.90	242.00	242.00	241.95	
4	14	1097-10	245.55	245.55	245.55	245.50	
4	15	1097-9	249.20	249.25	249.20	249.25	
4	16	1097-5	246.25	246.25	246.25	246.20	
4	17	1236-10	249.60	249.70	249.65	249.65	
4	18	1236-11	254.60	254.65	254.60	254.65	
4	19	1236-1	250.50	250.45	250.50	250.55	
4	20	1097-6	255.75	255.80	255.75	255.75	
calib.	1	1000 µm	1000.30	1000.30	1000.30	1000.25	11:30
calib.	3	500 µm	500.00	500.00	500.00	499.95	
calib.	5	250 µm	249.95	250.00	249.95	249.95	
calib.	7	100 µm	100.10	100.10	100.10	100.10	
calib.	9	0 µm	-0.05	-0.05	0.00	-0.05	
calib.	10	1375-19	746.95	746.95	746.90	746.90	(slp)
5	1	matrix	77.95	77.95	77.95	77.95	
5	2	matrix	72.30	72.35	72.30	72.35	
5	3	matrix	74.25	74.20	74.25	74.25	
5	4	matrix	76.75	76.75	76.75	76.75	
5	5	matrix	50.05	50.10	50.05	50.05	
5	6	matrix	50.95	50.95	50.95	50.95	
5	7	matrix	77.30	77.25	77.30	77.30	
5	8	matrix	75.60	75.60	75.60	75.60	
5	9	matrix	60.70	60.75	60.75	60.75	
5	10	matrix	61.60	61.60	61.60	61.60	
—		0 µm	-0.05	0.00	0.00		
5	11	matrix	55.05	55.05	55.05	55.05	
5	12	matrix	55.35	55.35	55.35	55.35	
5	13	matrix	76.60	76.60	76.60	76.65	
5	14	matrix	73.70	73.70	73.70	73.70	
5	15	matrix	77.45	77.45	77.50	77.45	
5	16	matrix	76.10	76.10	76.10	76.15	
5	17	matrix	57.00	57.00	56.85	56.95	bad touch (sig,slp)
5	18	matrix	59.55	59.65	59.45	59.35	bad touch (sig,slp)
5	19	matrix	79.50	79.55	79.55	79.55	
5	20	matrix	56.00	56.00	56.00	56.00	
calib.	1	1000 µm	1000.25	1000.25	1000.25	1000.25	12:00
calib.	3	500 µm	499.90	499.90	499.90	499.90	
calib.	5	250 µm	249.95	249.95	249.95	249.95	
calib.	7	100 µm	100.05	100.05	100.05	100.05	
calib.	9	0 µm	-0.05	-0.05	-0.05	-0.05	
calib.	10	1375-19	747.75	747.75	747.75	747.75	
1	1	1280-21	962.20	962.20	962.20	962.20	(rep)
1	2	1021-10	984.10	984.10	984.10	984.15	
1	3	1280-3	965.35	965.00	965.00	964.90	loose in mount (sig,slp)
1	4	1280-15	969.40	969.45	969.40	969.40	
1	5	1141-1	979.60	979.60	979.60	979.60	
1	6	1021-14	971.85	971.90	971.90	971.95	
1	7	1020-10	975.60	975.60	975.55	975.60	
1	8	1141-2	975.45	975.50	975.50	975.50	
1	9	1280-9	973.95	974.00	973.95	974.00	
1	10	1259-2	984.80	984.80	984.80	984.80	
—		0 µm	0.00	0.00	0.00		
4	1	1183-10	99.20	99.25	99.30	99.20	
4	2	1303-8	102.30	102.35	102.30	102.35	
4	3	1183-3	94.60	94.65	94.60	94.65	
4	4	1083-9	100.50	100.50	100.50	100.55	
4	5	1083-7	101.20	101.20	101.25	101.25	
4	6	1183-7	99.50	99.60	99.55	99.50	
4	7	1303-20	100.45	100.50	100.45	100.50	(rep)
4	8	1303-2	99.50	99.60	99.60	99.55	
4	9	1083-8	100.15	100.05	100.05	100.10	
4	10	1183-2	99.10	99.15	99.15	99.15	
calib.	1	1000 µm	1000.30	1000.30	1000.25	1000.30	12:40
calib.	3	500 µm	499.95	499.95	499.95	499.95	
calib.	5	250 µm	250.00	250.00	250.00	250.00	
calib.	7	100 µm	100.10	100.15	100.10	100.10	
calib.	9	0 µm	-0.05	-0.05	-0.05	-0.05	
calib.	10	1375-19	747.25	747.25	747.25	747.25	
1	20	1145-4	1010.90	1010.85	1010.90	1010.90	
2	10	1342-20	796.20	796.25	796.20	796.25	
2	20	1279-8	915.15	915.15	915.15	915.10	
3	10	1111-21	481.95	482.00	482.00	482.00	
3	20	1098-9	507.80	507.80	507.75	507.80	drags on pin
4	20	1097-6	255.65	255.65	255.70	255.65	
5	10	matrix	61.55	61.60	61.60	61.60	
5	20	matrix	56.00	56.05	56.05	56.00	
—		0 µm	-0.10	-0.10	-0.10		

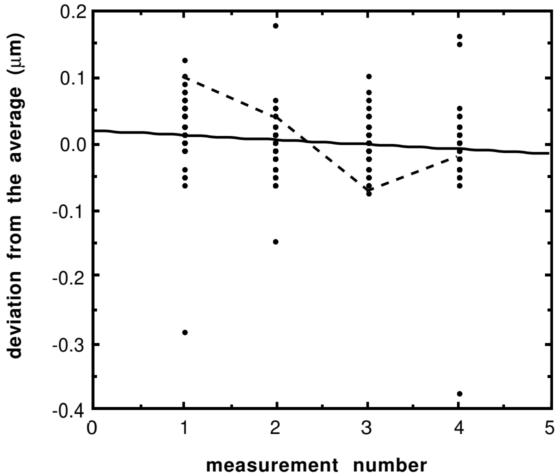

Figure 6. Deviations from the 4-measurement averages. (The downward trends indicate that shards appeared to get thicker with each probe hit.) Cuts are to be applied on data sets with outliers. The solid line follows the mean slope for all the shard measurements. The dotted line follows one data set with a rate of change that is considered to be too large.

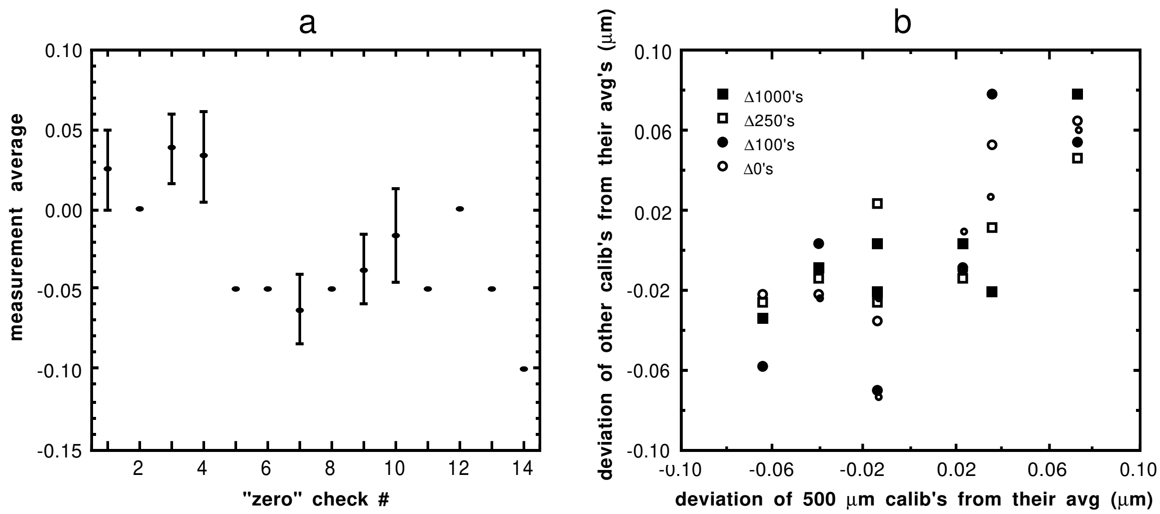

Figure 7. Progress of the calibrations. (a) "Zero" appears to have shifed downward by about 0.075 µm after check #4. (b) The gauge blocks tended to follow each others' trends as well as the "zero" shifts.

specification (µm)	average meas. (µm)
100.03 +0.?? -0.??	100.136 ± 0.028
250.01 +0.03 -0.03	250.003 ± 0.027
499.98 +0.00 -0.02	499.991 ± 0.026
1000.03 +0.07 -0.03	1000.311 ± 0.034

Table 2: Mitutoyo gauge block comparisons. The first and second errors in the specification are the maximum and minimum deviations from the central value. Errors for the "100 µm" gauge block were not reported. The manufacturer used a comparitor to make their measurements, which typically consists of two opposing probes that are much like the Heidenhain CERTO. The measured averages are compensated for "zero" shifts, and represent 28 measurements apiece.

The system linearity can now be checked by comparing the measured gauge block thicknesses with manufacturer's specifications: see Table 2. Discrepancies could be due to nonlinearities or metering inaccuracies, badly reported gauge block thicknesses, surface crud that was not cleaned away, or tilts. In fact, the 1000 and 100 μm gauge blocks were visibly tilted, possibly by enough to account for their disagreements. Regardless of the source of discrepancy, we remain close to or below the desired 0.1% level of uncertainty for all measurements if we treat the system linearity as exact.

The extra silicon shard in the calibration carrier was sampled seven separate times; i.e. it sustained more than 30 probe hits. This was done to assess whether silicon would start to crumble or crack. While there was no indication of any trend, the rms deviation was ≈ 0.53 μm, and the measurements bounced around by as much as 1 μm. This scatter is much larger than that seen in the repeatability checks performed on other shards. The cause is unknown. Later, it was found that this shard was tilted by over 1.5°, which was a relatively large amount that correlated with problematic measurements.

We will note five more items of calibration interest before proceeding to the initial comparisons of shard thickness with residual energy. (1) The temperature was held constant throughout these measurements. Nevertheless, tests were performed to try to induce thermal-expansion effects, but none were conclusively observed. (2) We tried to measure fingerprints, evaporating alcohol, and breath deposited on some shard surfaces, but no significant effects could be discerned. The round probe and pin tips presumably drove through any such fluid, so no wringing ambiguities should have occured, as expected. (3) We tried using less measuring force (1 N and 1.25 N) than the maximum allowed, and saw no effect. (4) We purposely tilted a couple shards out of their slots to check whether our setup proceedure was finely controllable. On a 1000 μm shard we obtained a 4 μm increase in thickness when the drive screw was rotated by 1/8th of a turn beyond the usual "touch" point. The reflections seen on that shard surface moved considerably. (Typically, screw rotations could be controlled to well within ~ 1/64th of a turn.) We then drove the carrier all the way down on the steel fixture, tilting the shard dramaticaly. When this carrier was released and reset and another measurement attempted, the original shard thickness was obtained: i.e. the flexing or tilting was not hysteretic. (5) Our measurements for shard thicknesses averaged 3.7 ± 7.5 μm smaller than those reported by Micron Semiconductor Ltd.. Using MSL's numbers gave much worse fits to the residual energies.

RESIDUAL ENERGY MEASUREMENTS AND INITIAL COMPARISONS

When plotted in stage -plus- MWPC coordinate space, residual energy data for each shard showed that over 99 % of the penetrating ^{36}Ar nuclei were located within a spot of radius 3.5 mm. (Each collimator hole in the shard carriers was about 2.4 mm in diameter, and the MWPC spatial resolution was roughly 1 mm.) Spots number 1 - 10 and 11 - 20 were spaced 7.6 mm apart. Bruce's first cut, therefore, was to ignore all events farther than 3.5 mm away from the center position of each spot. He then cropped the outlying data in energy space: eliminating events with energies more than four rms deviations from the mean. Between 3000 and 6000 events remained for each shard. He then fit a Gaussian and reported the residual energy at the peak (E') and the standard deviation (σ).

Bruce also fit a plane in energy-position space, giving $E' = Ax + By + E_o$ for each shard. Finally, he reported the (x,y) location of all spot centers, as well as the energies recorded there. These fits were made to assess how sensitive the correspondence would be between E' and thickness, t. If large gradients existed, then an accurate t(E') calibration would depend on just where we probed the shard.

The initial t-E' correspondence is shown in Figure 8. In general, error bars are smaller than the dot sizes. In (c), the cases where two dots are visibly separated by a small amount display the worse repeatability of our thickness measurements: all the ~ 100 μm shards were sampled twice. The solid lines in 8b and 8c are least-square fits to the data. Outliers (chosen by eye) are designated with square points, and were excluded from these fits. The dotted-line calculations are also very nearly linear, and were made using Hubert, Bimbot and Gauvin's (ADNDT **46**, 1-213, 1990) range-energy tables. These latter predictions were not based on any knowledge of the incident energies, but were normalized with respect to the average thicknesses and energies shown.

The scatter apparent in 8c may be due to many factors, including (1) surface crud. (2) It is very unlikely that the ^{36}Ar beam energy varied by ~ 1 MeV from shard to shard; but entrance foil uniformity and gain maps across the E' detectors could have had structure. (3) Scatter could be traced to the combined effects of (a) bad correspondences between the locations of mechanical thickness measurements and the average beam penetration points, and (b) large t or E' gradients; i.e. wedge-shaped shards or varying energy profiles across the beam spot. (4) The shards were visibly tilted on their carriers in many directions and by differing degrees. Figure 9 shows the size of discrepancies to be expected between mechanical and beam-determined thicknesses. (5) A history of changes, like tilt migrations or impact effects could lead to geometrical differences between the currently measured shards and those encountered by the beam.

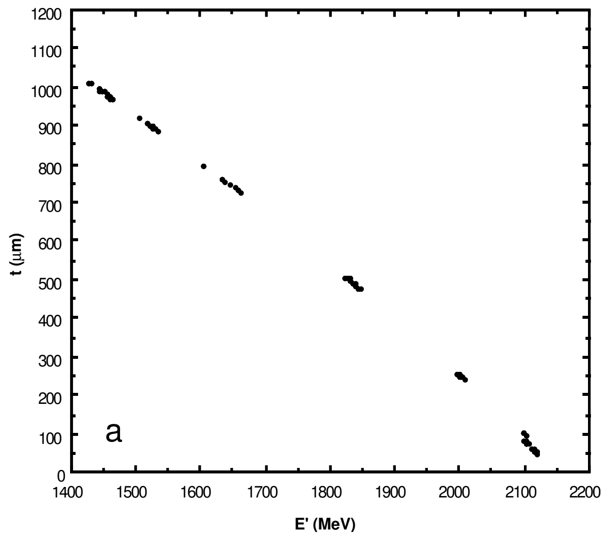

Figure 8. Shard thickness versus residual energy. (a) All uncut data. Mismatches at lower right arise from the extra 3.6 cm of beam path (air) inserted for matrix shards. (b) and (c) Expanded views of 1000 µm and 100 µm regions. Solid lines and inset equations are for linear fits. Square points indicate outliers that were excluded in these fits. Dotted lines are predicted trends using the 1990 Hubert etal. range-energy tables, normalized to the average energies and thicknesses shown in each region.

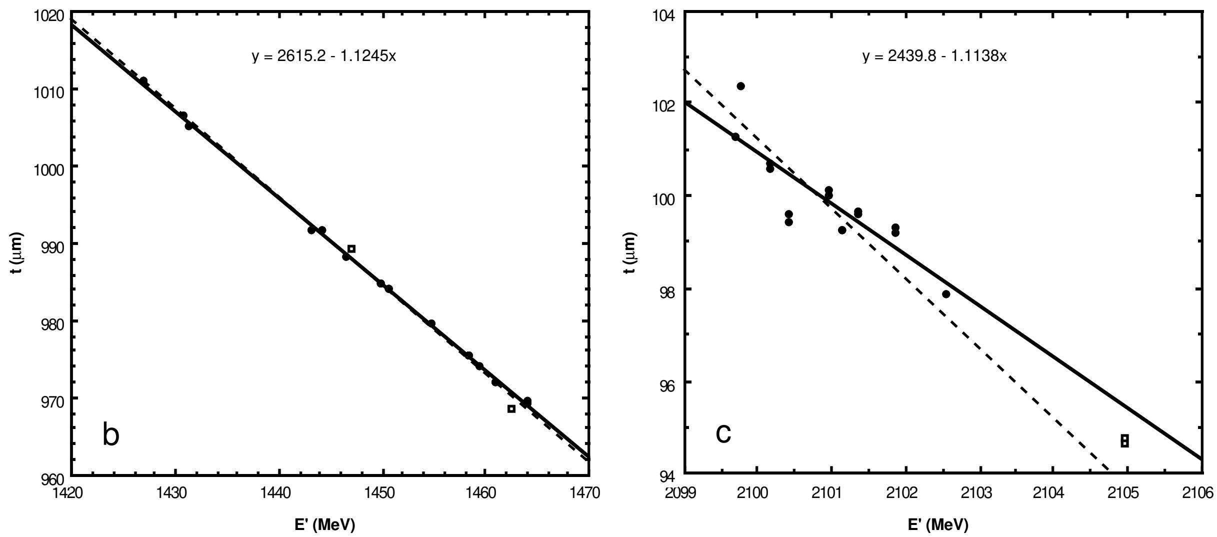

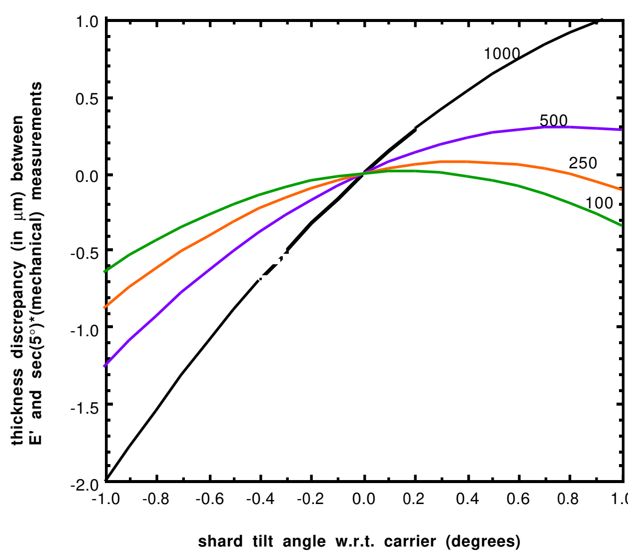

Figure 9. Difference between t*sec(5°+θ) and t*sec5°[1 + (secθ – 1)(r+R+t)], where θ is the tilt, r = 1.5 mm, and R = 1.7 mm. Different nominal shard thicknesses label the curves (with units of µm). Note that for 100 µm shards, any tilt leads to over-estimated mechanical thicknesses w.r.t E'-determined measurements, whereas for 1000 µm shards the discrepancy may change sign with the tilt direction.

TILTS

Shown in Figure 10 is the simple device used to measure shard tilts: 10b outlines the theory. A shard is aligned beneath the reference mirror, which in turn is adjusted to be normal to the line of sight as constrained by the eye guide. One sees a split image of the ruler in both shard and mirror, with a shift in rulings that is proportional to the shard tilt. A precision of 0.05° was maintained.

Tilts were measured both across the long (x) and short (y) axes of the shards: i.e. along directions that contribute differently to discrepancies between mechanical and E'-derived thicknesses. With a total tilt angle of $\theta \approx (\theta_x + \theta_y)/\sqrt{2}$, the actual shard thickness becomes $t \approx t_m - (\sec\theta - 1)(r+R+t_m)$, where t_m is the mechanically measured value. The ^{36}Ar beam penetrated an effective thickness of $t^*\sec(5°+\theta_y)\sec\theta_x$.

Tilts were also measured on both sides of each shard. Any difference could be interpreted as a wedge-shape. The average θ_x and θ_y tilts were used to calculate effective thicknesses. Some results are shown in Figure 11.

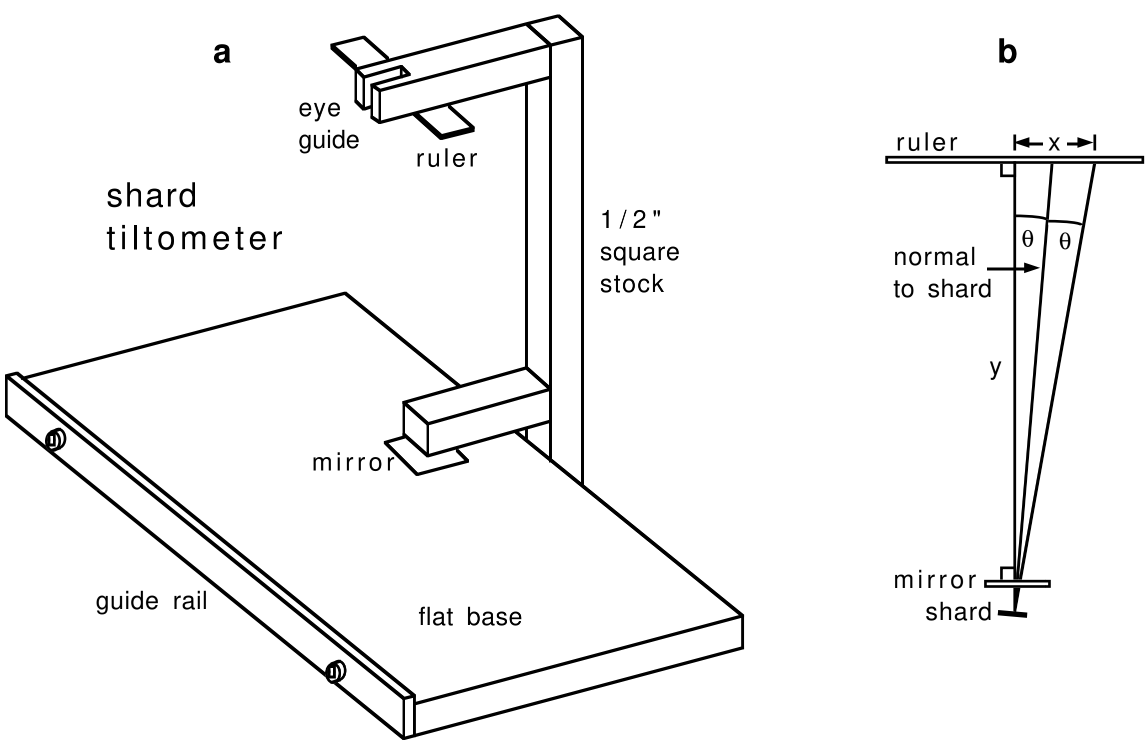

Figure 10. (a) The device used to measure shard tilts. The ruler is imaged at the same time in the shard and reference mirror. (b) A tilt of θ shifts images by $x \approx 2y\sin\theta$. If $y \approx 5^3/4$" then every 0.1° increase in θ leads to a shift in x by 0.02", or twice the ruling pitch.

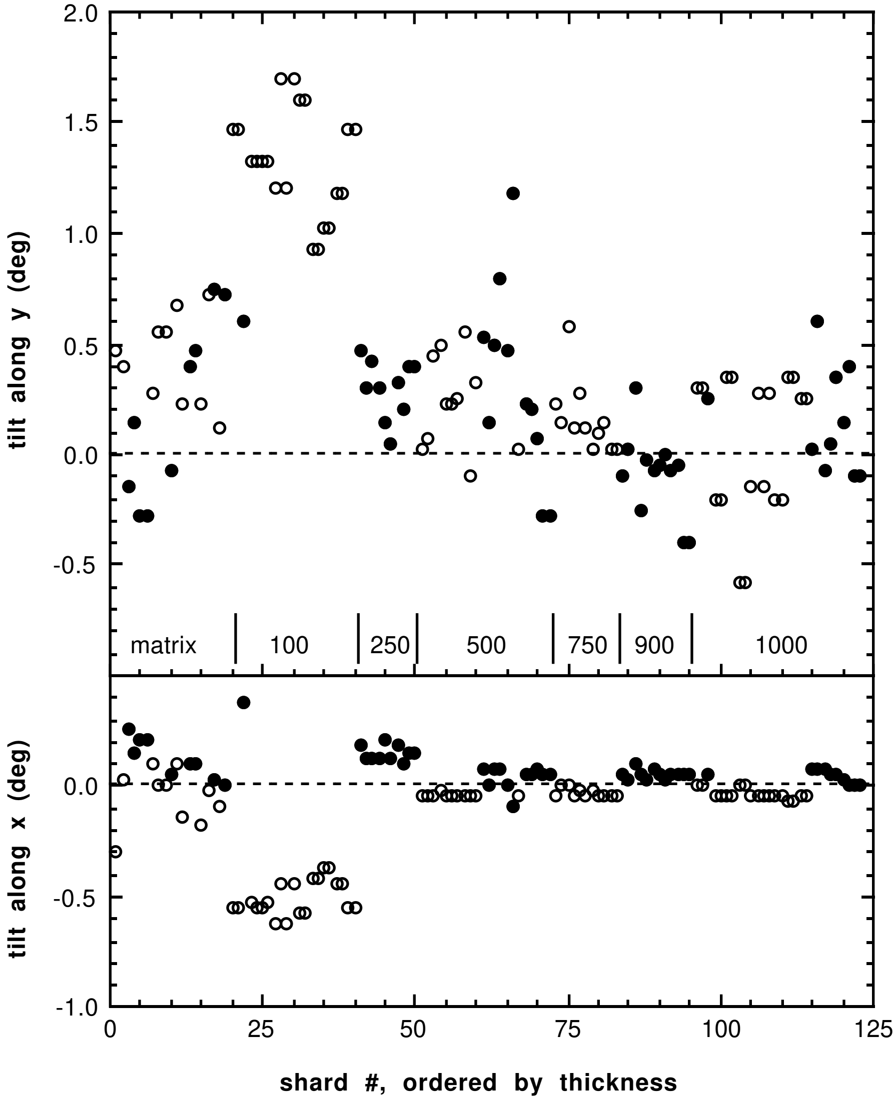

Figure 11. Shard tilts w.r.t. their carriers. Open circles are for shards in slots 1-10: closed circles for shards in slots 11-20. The y axis runs through carrier holes 1-10 and 11-20; i.e. it is rotated nominally 5° w.r.t. the Ar beam. The x axis is perpendicular to the beam. The angles plotted here are averages of those measured on both sides of each shard.

Except for a few shards in slots 11-20, the θ_y angles tended to be positive; i.e. most shards were tilted more than 5° with respect to the ^{36}Ar beam. The sign of θ_x angles systematically varied with slot number. All shards tended to tilt down toward the central rail of their carrier (between slots 1-10 and 11-20 as viewed from above as in Figure 2).

The θ_x and θ_y tilts measured on the oxide face of each shard typically differed by less than 0.15° from those measured on the aluminum face. For only two shards did these angles differ by 0.20° and 0.25°, indicating slightly more wedge-shaped aspects. Four other shards were so twisted, or loose in their slots, that tilts could not be measured. Such problematic shards correlated with those that had already been eliminated from our analyses for reasons of large sigmas or slopes, bad touches, etc.. By avoiding tilt extremes, data for three extra shards were cut.

The gauge blocks were tilted as well. (No wedges were discernable, as expected.) Table 3 shows that the correspondence between manufacturer's specifications and our adjusted measurements improved a little.

specification (μm)	tilt	adjusted meas. (μm)
100.03 +0.?? -0.??	0.32°	100.085 ± 0.028
250.01 +0.03 -0.03	0.10°	249.997 ± 0.027
499.98 +0.00 -0.02	0.14°	449.980 ± 0.026
1000.03 +0.07 -0.03	0.14°	1000.298 ± 0.034

Table 3: Gauge block thickness comparisons, after accounting for tilts.

When corrected for tilts, the scatter in (E',t) space shown in Figures 8b and 8c improved only a little. The major source of these discrepancies must be found elsewhere.

A history of shard movements and surface altrations cannot be ruled out. The loaded carriers were transported across country, jostled by hand, and subjected to many environmental changes during the year between MSU and our latest measurements. Since the effects induced are unknown, they are also irreproducible. We can report, however, that close visual inspection revealed tiny markings due to probe impacts on the aluminum faces of some shards. The harder oxide faces were all clear of such markings. A smattering of tiny particles (dust?) was also observed. These features may account for some of the (E',t) scatter. But our thickness data showed very little variation among the four measurements made for each shard. And the cuts we made to eliminate questionable data are the same that would be expected to distinguish random dust or probe-impact difficulties. It is therefore improbable that such effects could lead to all the disparities.

Tilts might have changed. A shard that was flexed might get caught on the side of its slot, and not be able to spring back to its original position. Also, the silicone material that holds shards in place might have responded with hysteresis to pulls or twists. To check for these possibilities, we gently pushed on each shard and noted whether it sprung back. In general, shard orientations appeared to be completely restorable, but six "catching" cases were found, five of which were among the "100 μm" shards. These particular cases were reasonably well correlated with the outliers in Figure 8, and were therefore eliminated from the data.

E' GRADIENTS AND MAPS, AND FINAL RESULTS

Bruce's planar fits revealed large gradients along x, usually in the ~ 1 MeV/mm range. These could arise from (a) bad fits, (b) an unexpected beam-spot energy profile, or (c) wedge-shaped shards. [We note that the interferometry maps also showed wedges: but these latter may be IDL artifacts. Given the shard orientations with respect to the ^{36}Ar beam, such wedges would appear in our E' measurements as larger gradients along y, not along x.] Case (c) was ruled out with the tilt measurements. Case (b) could obtain if the beam passed through some nonuniformity, such as a wrinkle in the stack of aluminum foils used to degrade the beam energy. Indeed, this degrader appears quite wrinkly today. (I do not recall how it looked at MSU.) And Bruce confirms that there was a similar energy profile across the beam-spot even when there was no intervening shard in place. But whatever their origin, these gradients were systematic, not random. Moreover, the locations of our mechanical thickness measurements were constrained by the collimator hole -to- pin tolerance. Small systematic offsets may have resulted, but scatter in (E't) space due to this source is unlikely.

Beam-energy maps across the stopping detectors made without shards in place revealed variations of ± 1 MeV in E' response. These variations followed a roughly circular pattern, centered on the detector axis, which makes it unlikely that the beam energy itself was drifting. Such patterns appeared on both stopping detectors used, but in an uncorrelated way, so nonuniformities in entrance foil thickness were not the cause. A drop of ~ 1 MeV for a ~ 2200 MeV ^{36}Ar beam could be due to a gold degrader ~ 3000 Å thick. Since this exceeds the total thickness of gold deposited on the entrance faces of our Si(Li) detectors, dead layer variations are not to blaim. We are left to posit that the observed E' contours represent deviations of gain at different locations within the stoppng detectors. Such effects might be due to crystal morphology variations leading to charge recombination differences, though this is speculative. We nonetheless treated the relative variations as multiplicative efficiencies.

Locations of shard samples were then superimposed upon these maps, and the corresponding efficiencies are noted in Table 4. Energy shifts of ~ 1 MeV made a significant difference in the (E',t) fits, especially for the thinner shards. The improvement can be seen in Figure 12, and final fits are listed in Table 5. Linear fits to the data agree very well with predicted trends computed from the Hubert etal. range-energy tables. The accuracy is acceptable: except for the matrix shards (with which we are not quite so concerned) the rms deviations are at worst ≈ 0.4 % with respect to the nominal shard thicknesses.

slot#	stopping detector #8136	stopping detector #8138	slot#	stopping detector #8136	stopping detector #8138
1	0.99954	1.00000	11	0.99968	0.99995
2	0.99954	1.00000	12	0.99954	1.00000
3	0.99954	0.99995	13	0.99954	1.00005
4	0.99954	0.99995	14	0.99907	1.00000
5	0.99954	1.00005	15	0.99907	0.99995
6	0.99986	1.00000	16	0.99907	0.99995
7	0.99954	1.00000	17	0.99907	0.99995
8	0.99935	1.00000	18	1.00000	1.00000
9	0.99954	1.00042	19	0.99954	0.99977
10	0.99954	1.00000	20	0.99954	1.00005

Table 4. Relative stopping-detector gains at the various shard locations. Detector #8136 was used for carriers 1 and 4, while #8138 was used for carriers 2, 3 and 5. The generally lower #8136 numbers were visible in the E' maps, and since the mapping runs for #8136 and #8138 were consecutive, these numbers were treated here as gain differences, and not due to beam energy drifts.

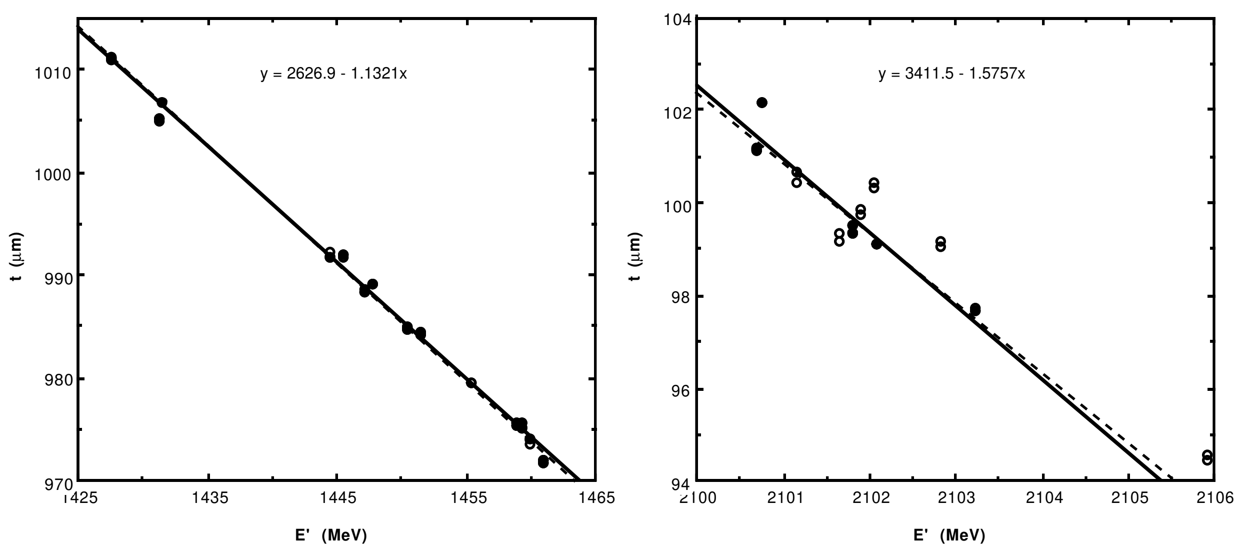

Figure 12. Shard thickness (in the 1000 and 100 μm regions) versus residual energy after all the cuts are taken and adjustments made. Comparisons should be made with Figures 8b and 8c. Open circles: data that was cut for various reasons. Outliers from the lines were not arbitrarily cut. Closed circles: surviving data, used to make the fits. Solid lines: linear fit to the data. Dashed lines: predicted trends using Hubert etal., normalized to the average thicknesses and energies shown. The correspondence between fits is equally good in all other thickness regions.

			linear fit to uncut data			prediction (about average)		
shards	#total	#cut	m	b	Δ	m	b	Δ
matrix	19	0	-1.5701	3379.5	0.714	-1.5216	3277.2	0.789
100	21	13	-1.5757	3411.5	0.381	-1.5143	3282.4	0.383
250	10	0	-1.4648	3183.9	0.887	-1.4669	3188.1	0.886
500	22	2	-1.3920	3045.8	0.931	-1.3712	3007.5	0.950
750	11	1	-1.2706	2837.7	0.743	-1.2607	2821.5	0.771
900	12	3	-1.1059	2582.3	0.956	-1.1938	2716.3	1.193
1000	28	6	-1.1321	2626.9	0.708	-1.1514	2655.0	0.747

Table 5. Final fits to the data. The total number of measurements available is listed as #total for shard thicknesses in the ranges of column 1, while the number of measurements cut is listed as #cut. (There were 8 surviving measurements of 5 separate shards used to fit "100 μm" data.) Fits are $t = m*E' + b$, where the rms deviation from the fit is listed as Δ. Units are μm and MeV throughout. The "prediction" is made using the Hubert etal. tables, normalized about the average thicknesses and energies available in each range.

These are our final results. Either the "prediction" or empirical fits to the data may be used to calibrate SIS detector thicknesses. Care must be taken to compensate for the apparent gain variations observed in the stopping detectors. The thickness fits listed above include the multiplicative sec5° increases.

CONSISTENCY CHECK WITH THE HUBERT ETAL. RANGE-ENERGY TABLES

As an auxiliary use of the above data, we performed an overall consistency check among the measured thicknesses, residual energies, and the Hubert etal. range-energy tables. Given the adjusted values for t and E' (and using data that survived cuts), we calculated the total energy incident on the front face of each shard. We accounted for the various air gaps that intervened between shards and stopping detectors. We also adjusted for the differences in energy observed in the beam monitor detectors. As can be seen in Figure 13, the incident energies deviated systematically with shard thickness. This deviation could be taken out by assuming the Hubert etal. ranges were marginally too high by an amount which increases as energies drop from ~60 to ~40 MeV/nucleon. A similar effect could be had by altering the gain, to suggest that the true residual energies were slightly higher than those recorded. Then the fault would not trace to the Hubert etal. tables, but to our experimental calibrations. We note however, that the actual incident energy was around 2172 MeV, as measured by a stopping detector without any intervening shard in place (and accounting for the airgap). To attain consistent results, offsets may have to be incorporated. Ambient MSU air pressure and temperature changes were not large enough to lower the spread. Clearly, the investigation of these discrepancies deserves more effort.

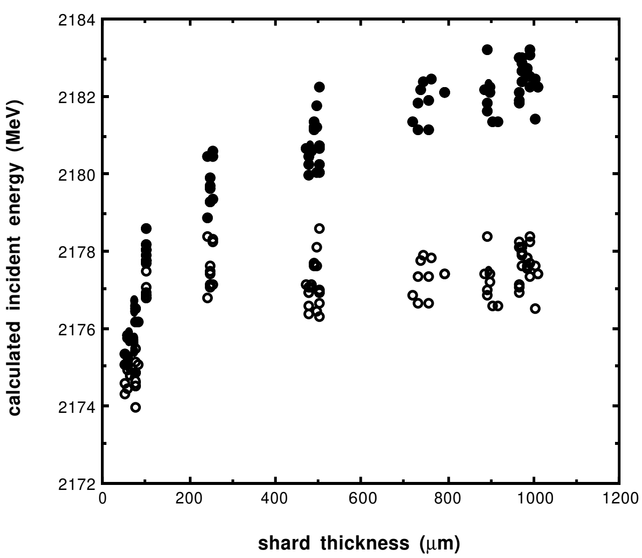

Figure 13. Consistency check among measured shard thicknesses, residual energies, and Hubert etal. range-energy tables. Solid circles: incident energies implied by the data. Open circles: after adjusting ranges down by the amount $\Delta R/R = 0.015 - 0.0000075*R$, or 0.2% at E = 2100 MeV, and 0.4% at E = 1400 MeV, apropo the 100 µm and 1000 µm shards respectively.